SUPPLEMENTARY INFORMATION

Uniquely Structured Composite Microspheres of Metal Sulfides and Carbon with Cubic Nanorooms for Highly Efficient Anode Materials for Sodium-Ion Batteries

Jin Koo Kim,[†a] Seung-Keun Park,[†b] Jin-Sung Park,[a] and Yun Chan Kang*[a]

[a] *Department of Materials Science and Engineering, Korea University, Anam-dong, Seongbuk-gu, Seoul 136-713, Republic of Korea. E-mail: yckang@korea.ac.kr*

[b] *Department of Chemical Engineering, Kongju National University, 1223-24 Cheonandaero, Seobuk-gu, Cheonan 31080, Republic of Korea*

[†] *These authors contributed equally to this work.*

Characterization

Structural and morphological analyses of the synthesized powders were performed using scanning electron microscopy (SEM; TESCAN, VEGA3) and field-emission transmission electron microscopy (TEM; JEOL, JEM-2100F). The crystal structures and phases were analyzed using X-ray diffraction (XRD; X'Pert PRO) with Cu-K$_\alpha$ radiation. The specific surface areas and pore-size distributions of the samples were estimated via Brunauer–Emmett–Teller (BET; TriStar 3000) analysis of nitrogen-adsorption measurements. The chemical states of the MoS_2/C-NR composite microsphere were confirmed using X-ray photoelectron spectroscopy (XPS; Thermo Scientific K-Alpha) with Al-K$_\alpha$ radiation (12 kV and 20 mA). The carbon content of the MoS_2/C-NR composite was determined via thermogravimetric analysis (SDT Q600), courtesy of Korea Basic Science Institute in Busan. Raman spectroscopy (LabRam HR800, Horiba Jobin-Yvon, excited by 515-nm diode laser) was conducted at room temperature to study the nature of the carbon and MoS_2 nanosheets of the MoS_2/C-NR composite.

Electrochemical Measurements

The sodium-ion storage performances of the synthesized samples were analyzed by assembling 2032-type coin cells. The anode material slurry was prepared via mechanical mixing of the sample powders (active material, 70 wt%), Super P® (conducting agent, 20 wt%), and sodium carboxymethyl cellulose (binder, 10 wt%) with a few drops of distilled water. To prepare the working electrode, the slurry was printed on a copper foil using a doctor blade and dried under ambient air. The mass loading of the mixture on the electrode was 1.4 mg cm^{-2} (diameter of the round electrode was 14 mm). Sodium foil was employed as the counter electrode. Microporous polypropylene film was employed as the separator. The electrolyte was prepared by dissolving 1 M of $NaClO_4$ in a 1:1 volume mixture of ethylene carbonate and

dimethyl carbonate (DMC) with 5 wt% fluoroethylene carbonate. Galvanostatic charge/discharge and cyclic voltammetry (CV) measurements were conducted using an electrochemical cycler (WonA tech) in the potential range of 0.001–3.0 V vs. Na^+/Na. Electrochemical impedance spectroscopy (EIS) was performed using a potentiostat/galvanostat (ZIVE SP1, WonA Tech) in the frequency range of 0.01 Hz–100 kHz. After the cycling performance tests, the cells were disassembled in an argon-filled glove box, and the working electrodes were removed and washed with DMC and dried in vacuum for the following characterizations.
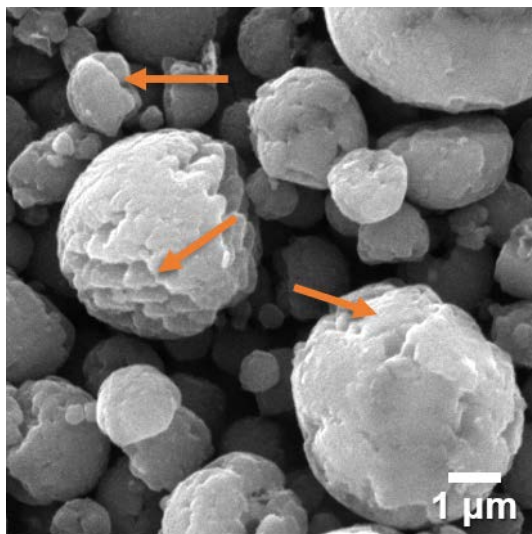
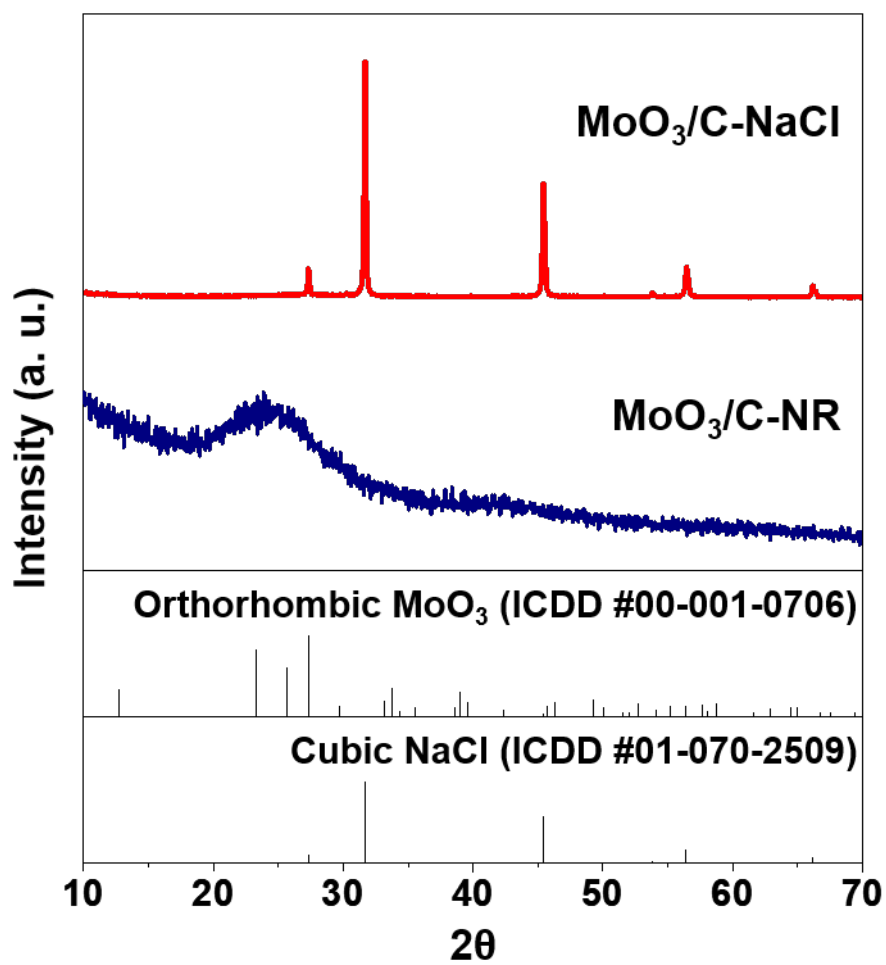**Fig. S1** SEM image of MoO$_3$/C-NaCl composite microspheres prepared via one-pot spray pyrolysis.

Fig. S2 XRD patterns of MoO₃/C-NaCl (before washing) and MoO₃/C-NR (after washing).
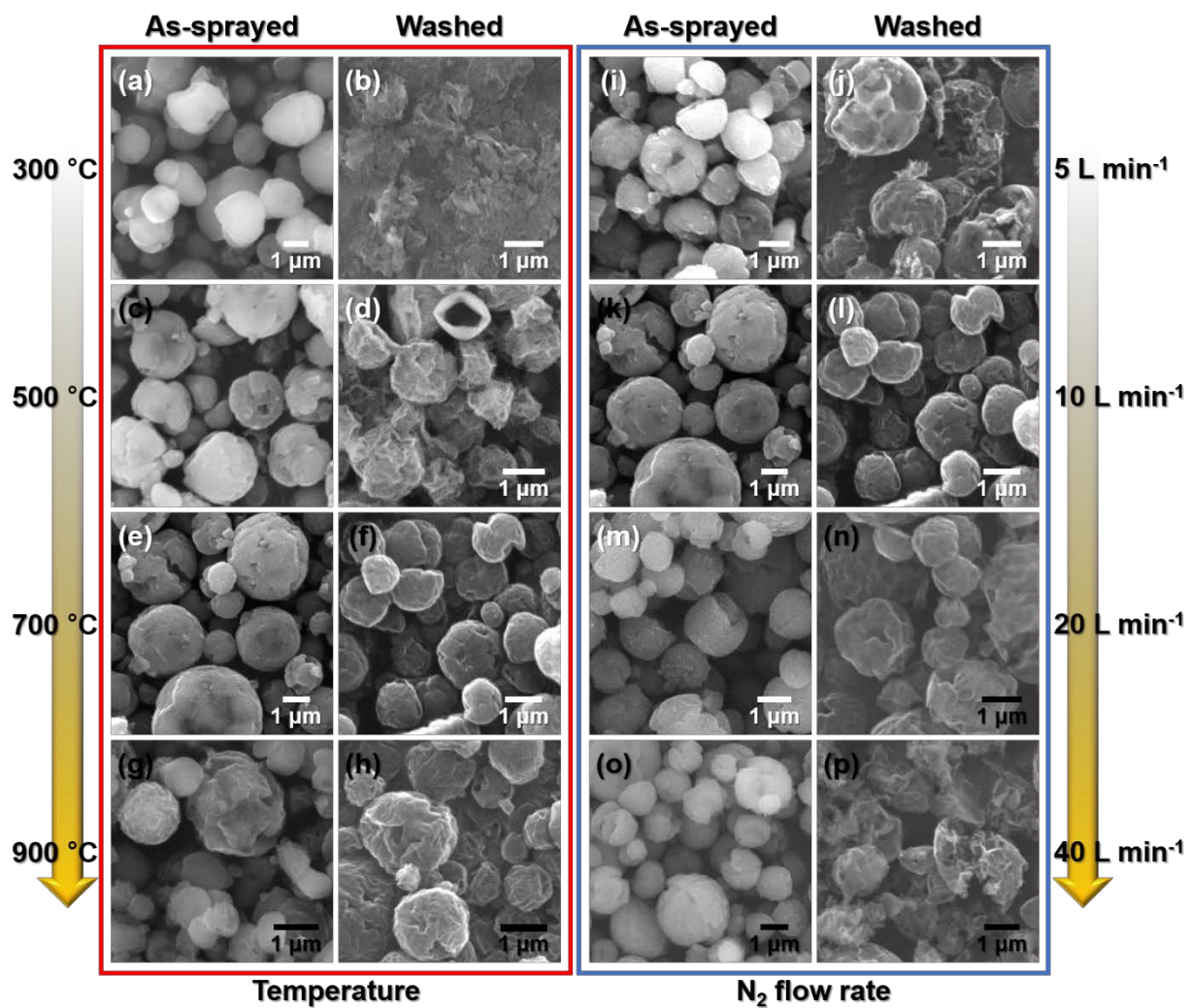
Fig. S3 Morphological change of MoO_3/C-NR upon the variation of (a-h) synthesis temperature and (i-p) N_2 flow rate.
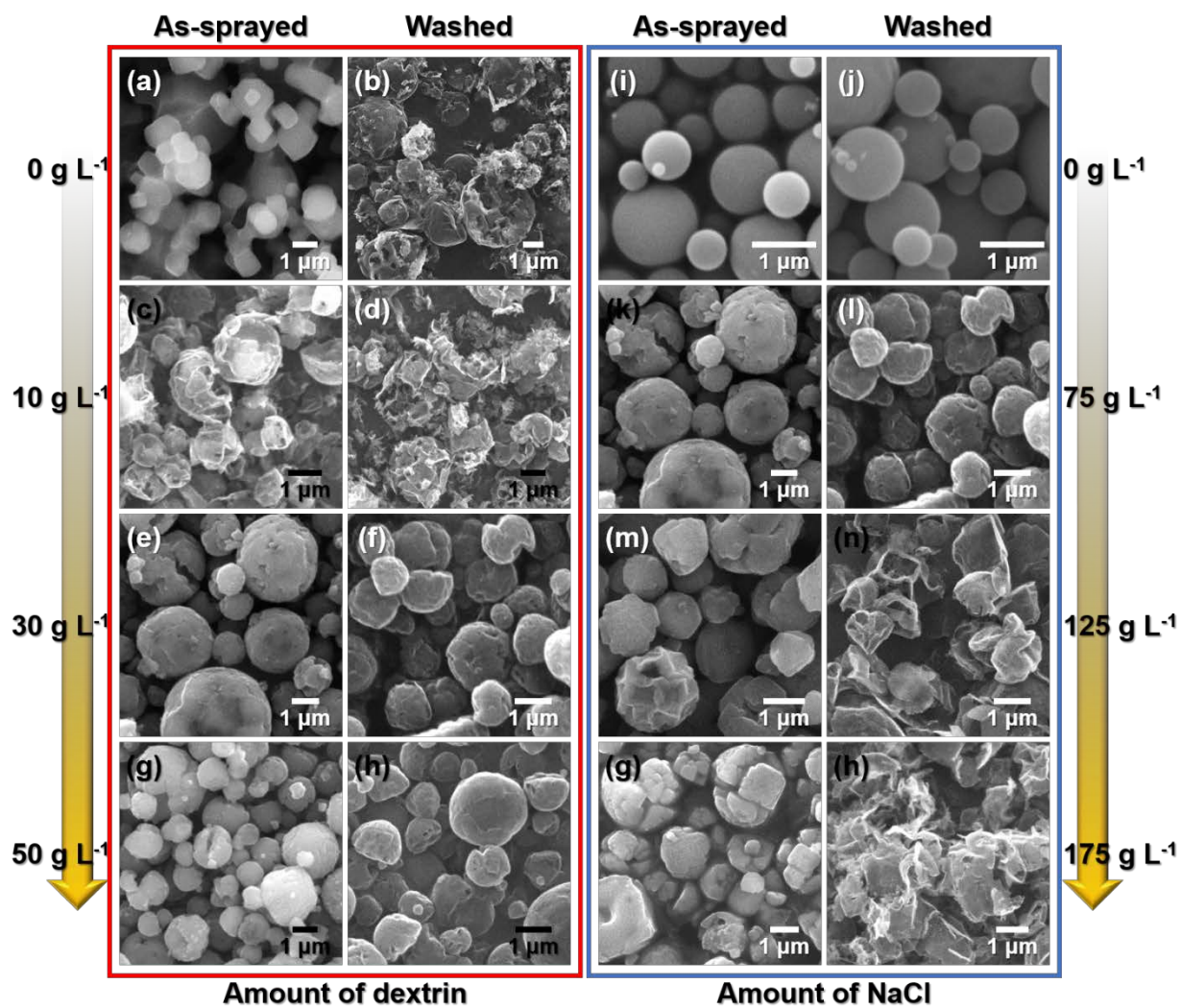
As-sprayed **Washed** **As-sprayed** **Washed**

(a) (b) (i) (j)

0 g L^{-1}

(c) (d) (k) (l)

10 g L^{-1}

(e) (f) (m) (n)

30 g L^{-1}

(g) (h) (g) (h)

50 g L^{-1}

0 g L^{-1}

75 g L^{-1}

125 g L^{-1}

175 g L^{-1}

Amount of dextrin **Amount of NaCl**

Fig. S4 Morphological change of MoO_3/C-NR upon the variation of (a-h) the amount of dextrin and (i-p) the amount of NaCl.

7

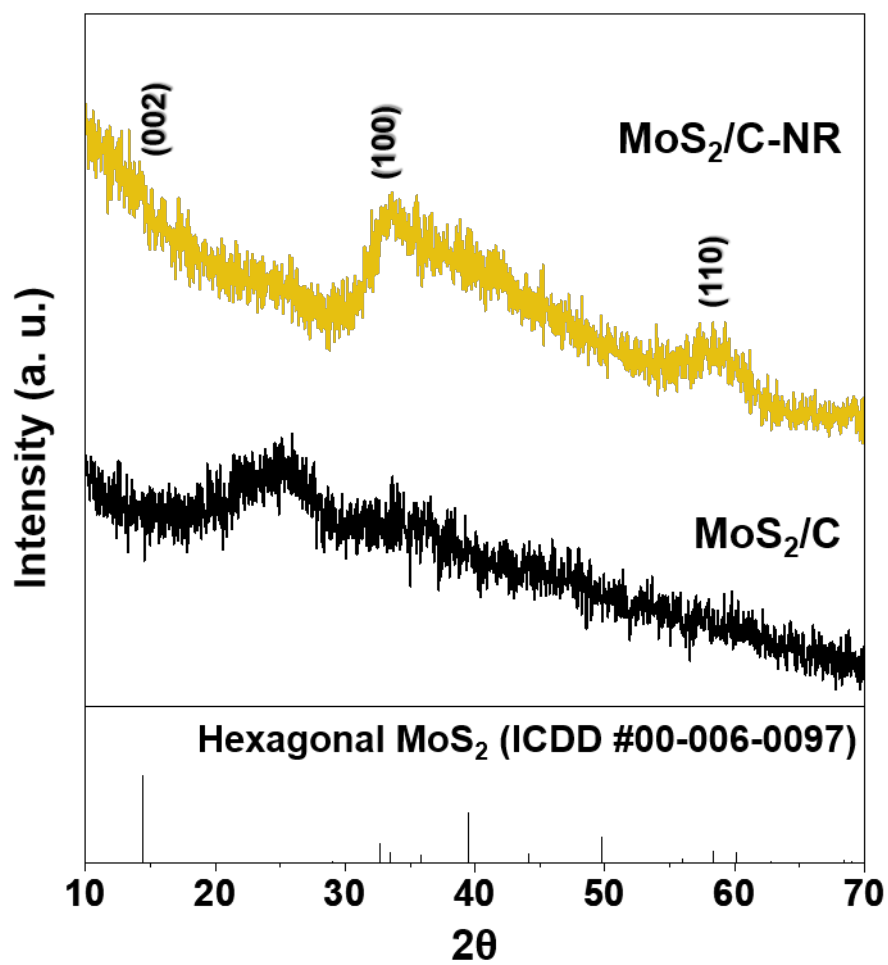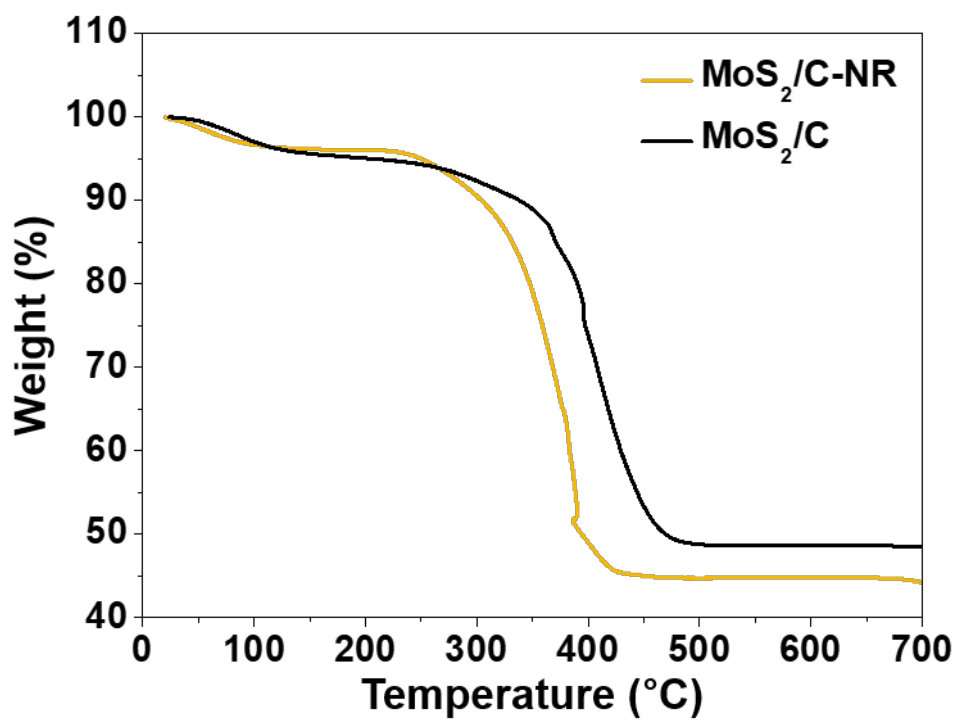**Fig. S5** XRD patterns of MoS$_2$/C-NR and MoS$_2$/C.

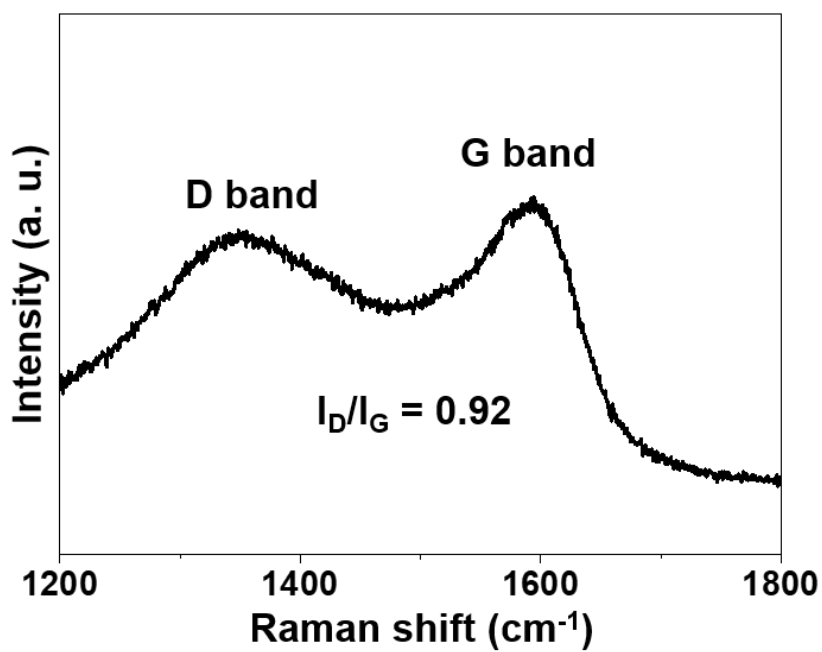**Fig. S6** TG curves of MoS$_2$/C-NR and MoS$_2$/C.

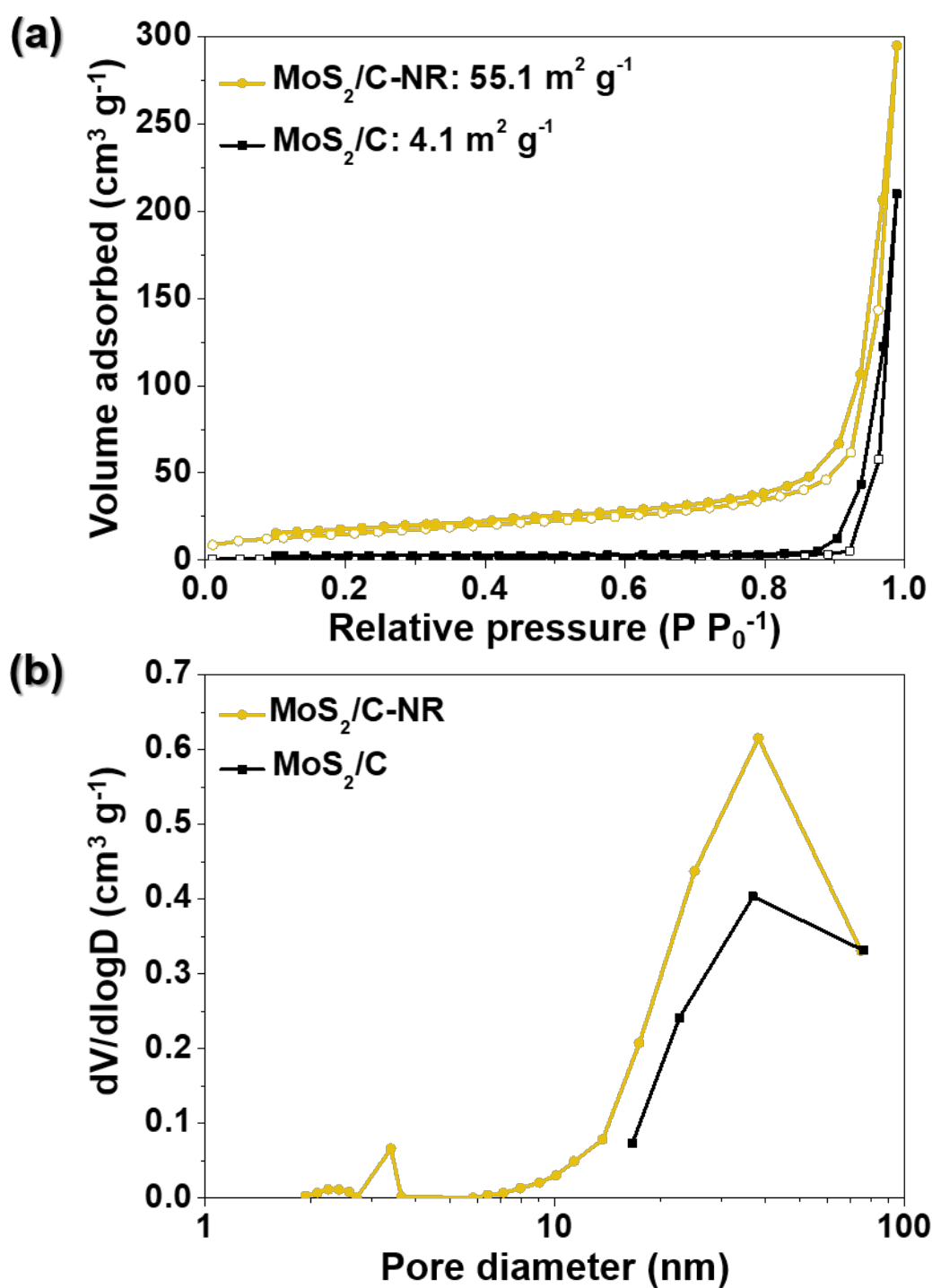**Fig. S7** Raman spectrum of MoS$_2$/C.

Fig. S8 (a) N_2 gas adsorption/desorption isotherms and (b) BJH pore size distributions of MoS$_2$/C-NR and MoS$_2$/C.
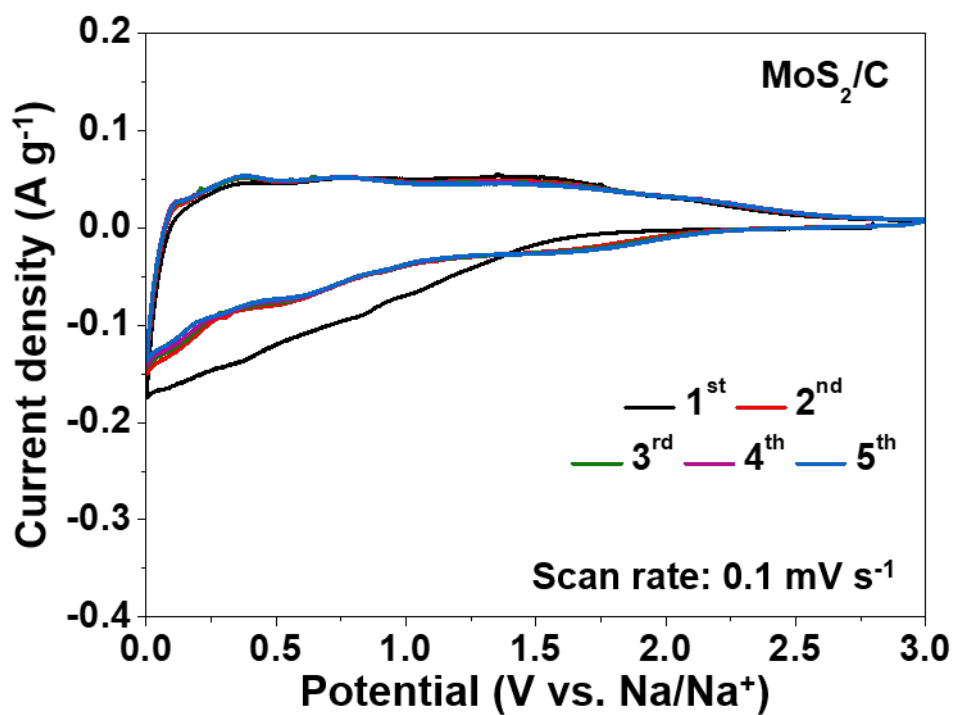
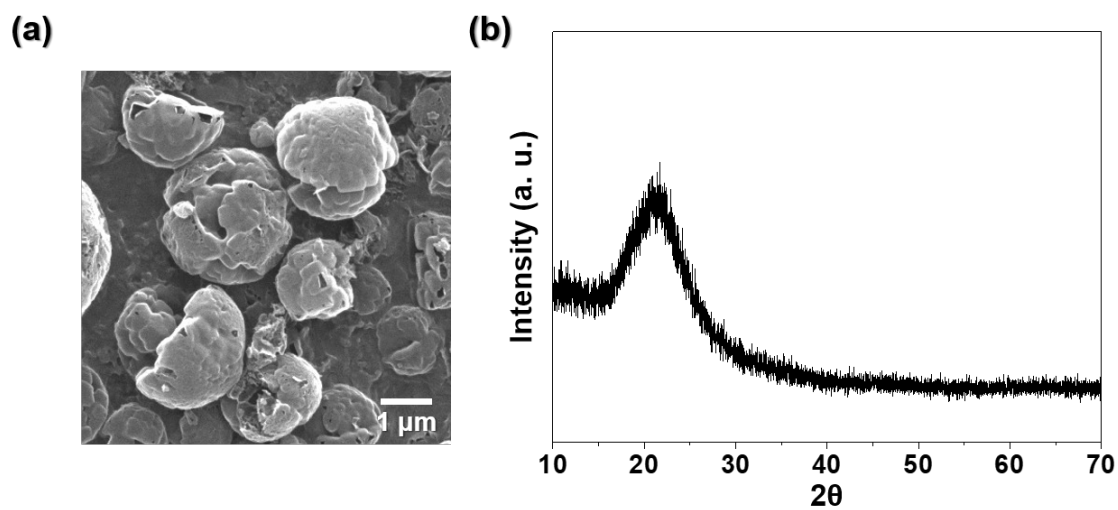**Fig. S9** CV curves of MoS$_2$/C for the initial 5 cycles.

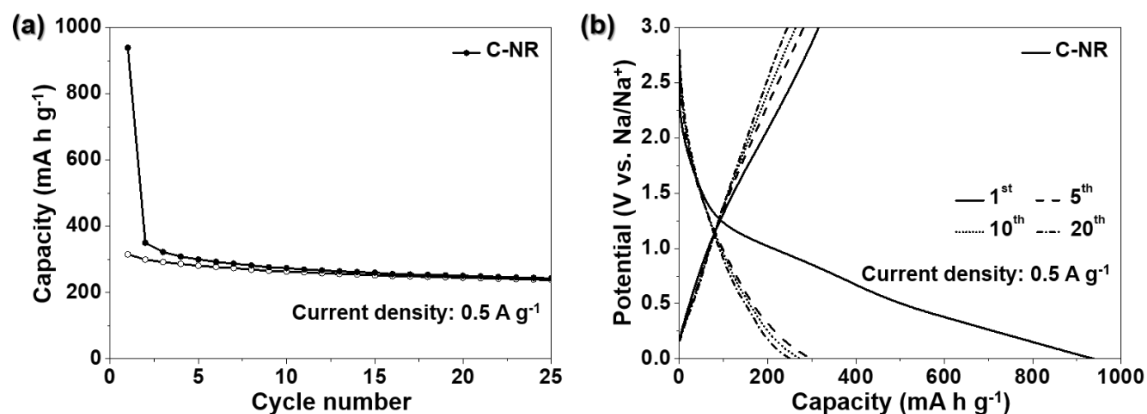**Fig. S10** (a) SEM image and (b) XRD pattern of C-NR.

Fig. S11 Sodium-ion storage performance of C-NR: (a) cycling performance at a current density of 0.5 A g^{-1} and (b) discharge-charge profiles.
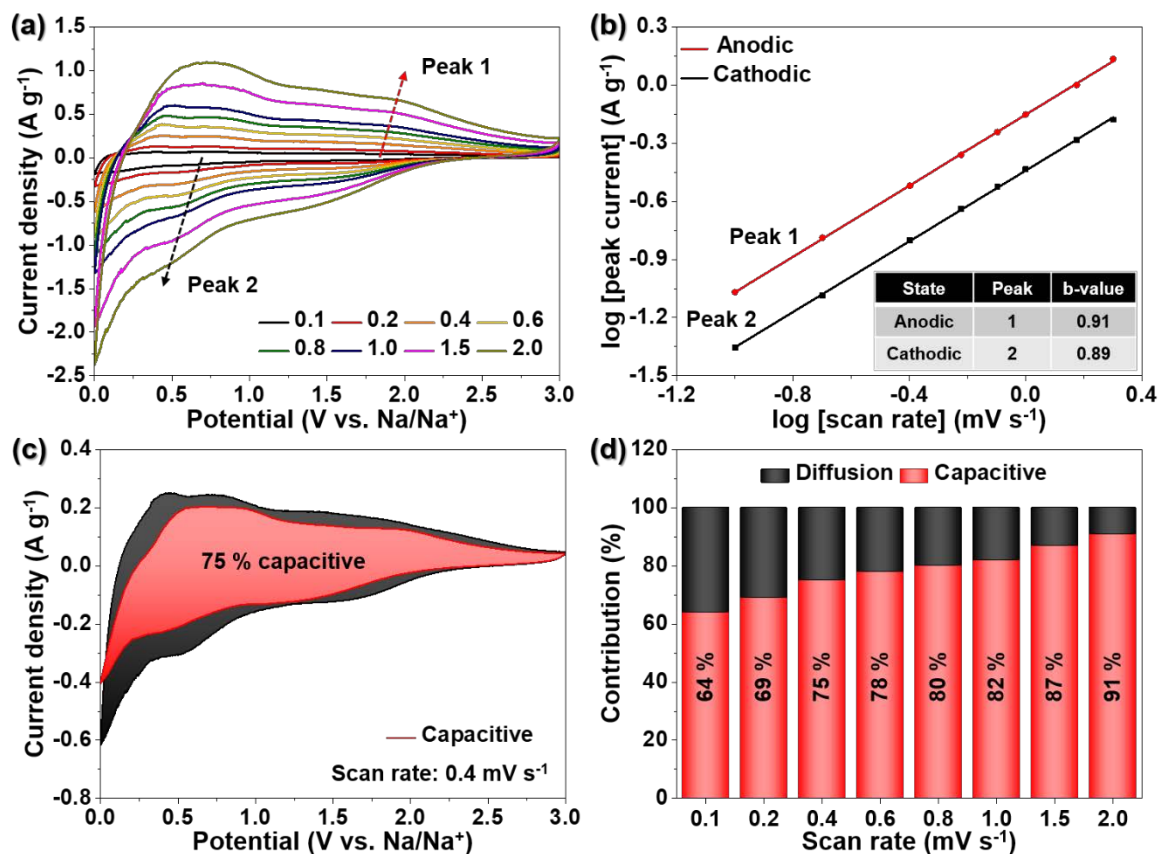

Fig. S12 Electrochemical kinetics analysis of MoS$_2$/C: (a) CV curves at various scan rates from 0.1 to 2.0 mV s^{-1}, (b) corresponding log (i) vs. log (v) plots at designated peak currents, (c) CV curve with the capacitive fraction (shaded area) at a scan rate of 0.4 mV s^{-1}, and (d) bar chart summarizing the capacitive contributions at various scan rates.
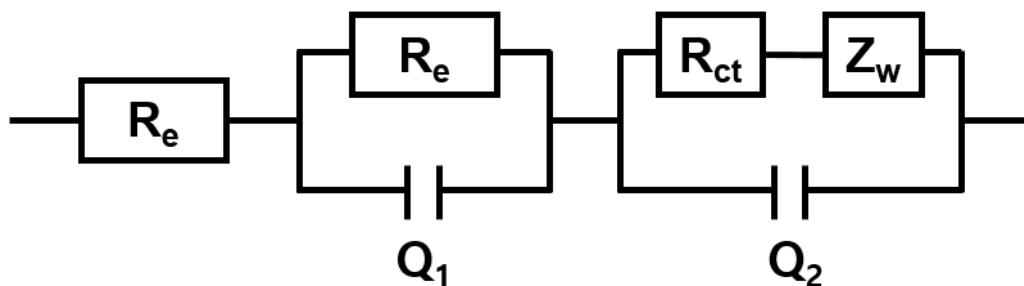
Fig. S13 Equivalent circuit model used for EIS.

R_e: Electrolyte resistance, corresponding to the intercept of high frequency semicircle at Z_{re} axis

R_f: SEI layer resistance corresponding to the high-frequency semicircle

Q_1: Dielectric relaxation capacitance corresponding to the high-frequency semicircle

R_{ct}: Charge transfer resistance related to the middle-frequency semicircle

Q_2: Associated double-layer capacitance related to the middle-frequency semicircle
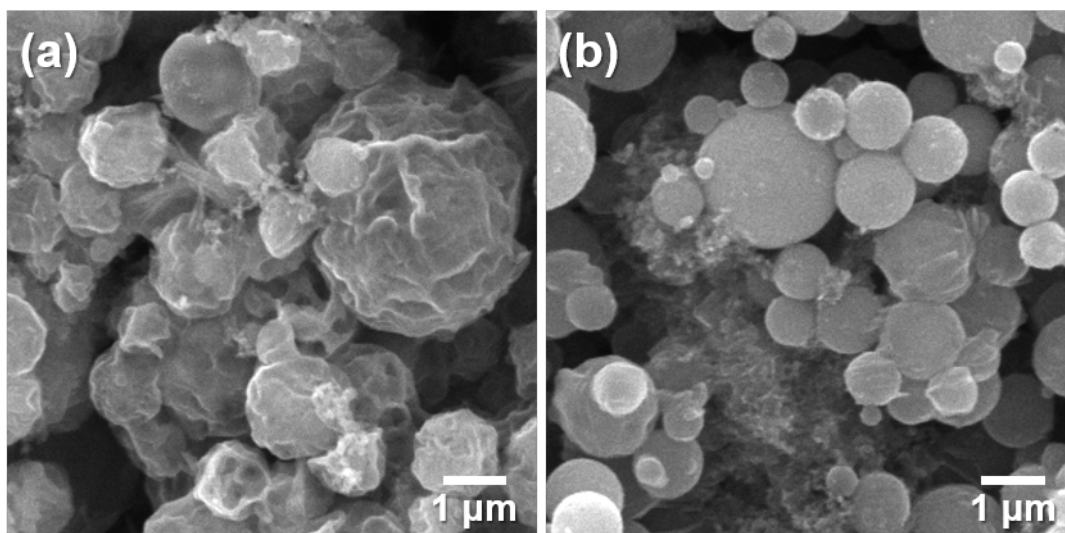
Z_w: Na-ion diffusion resistance

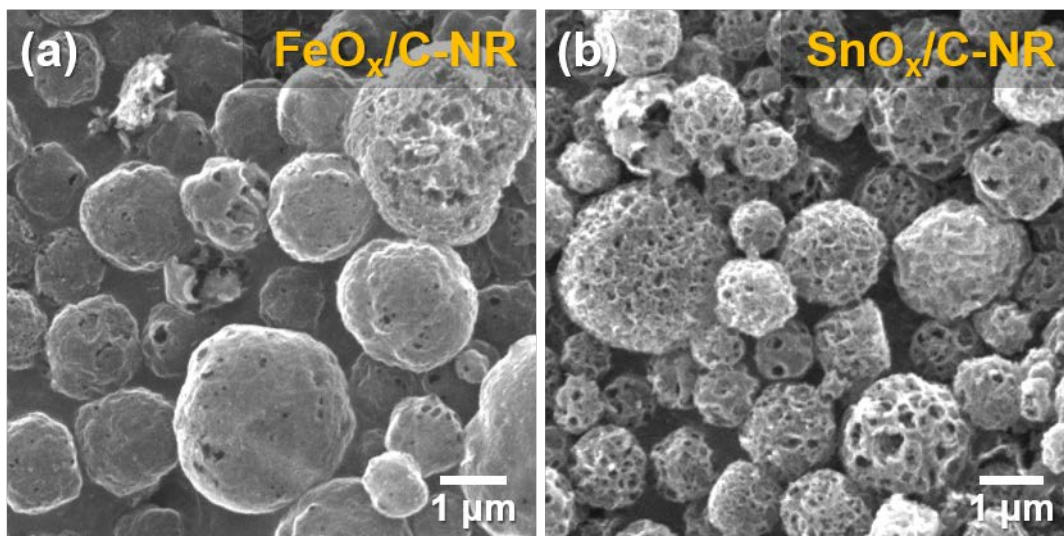**Fig. S14** SEM images of the electrodes obtained after 100 cycles: (a) MoS$_2$/C-NR and (b) MoS$_2$/C.

Fig. S15 SEM images of the MeO$_x$/C-NR powders: (a) FeO$_x$/C-NR and (b) SnO$_x$/C-NR.
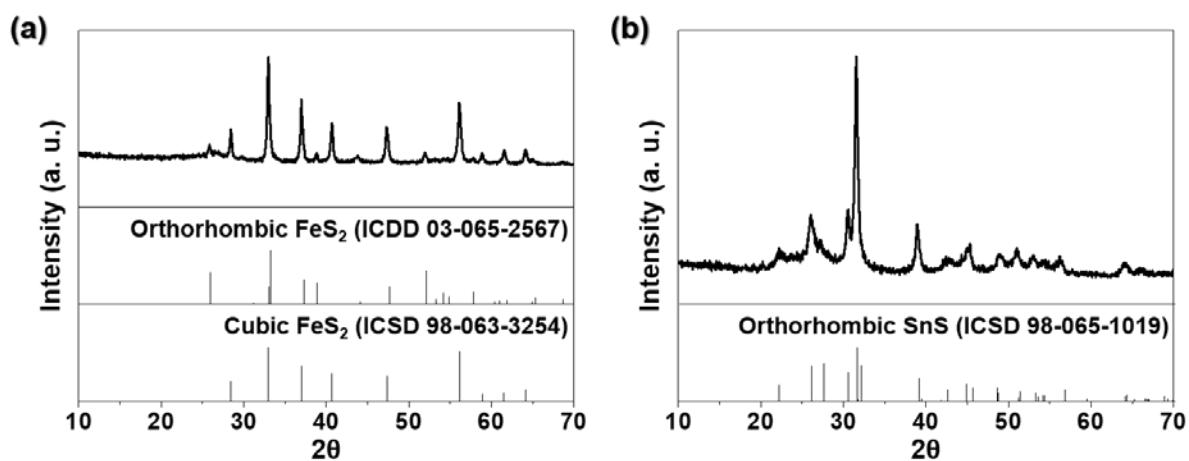

Fig. S16 XRD patterns of (a) FeS$_2$/C-NR and (b) SnS/C-NR.

Fig. S17 Sodium-ion storage performances of FeS$_2$/C-NR: (a) CV curves for the initial 5 cycles, (b) discharge-charge profiles, (c) cycling performance at a current density of 0.5 A g^{-1}, and (d) rate performance.

In the first cathodic scan of the CV graph of FeS$_2$/C-NR (Figure S12a), the reduction peaks at 1.02 corresponded to the Na$^+$ ion intercalation to FeS$_2$ to form Na$_x$FeS$_2$ (x < 2). The subsequent reduction peak at 0.37 and 0.27 V was attributed to the conversion reaction to form Fe nanocrystals and Na$_2$S matrix, along with the formation of SEI layer. For the anodic scan, the oxidation peaks at 1.29, 2.18 and 2.52 V corresponded to the desodiation process of Fe and Na$_2$S to form Na$_2$FeS$_2$ and further removal of Na to form Na$_{2-x}$FeS$_2$ (0 < x < 2). From the second cycle and onward, the reduction peak at 0.37 V disappeared, indicating that FeS$_2$ phase could not be recovered after the first cycle because of the irreversible formation of the SEI layer that preceded the conversion reaction.[S1,S2]
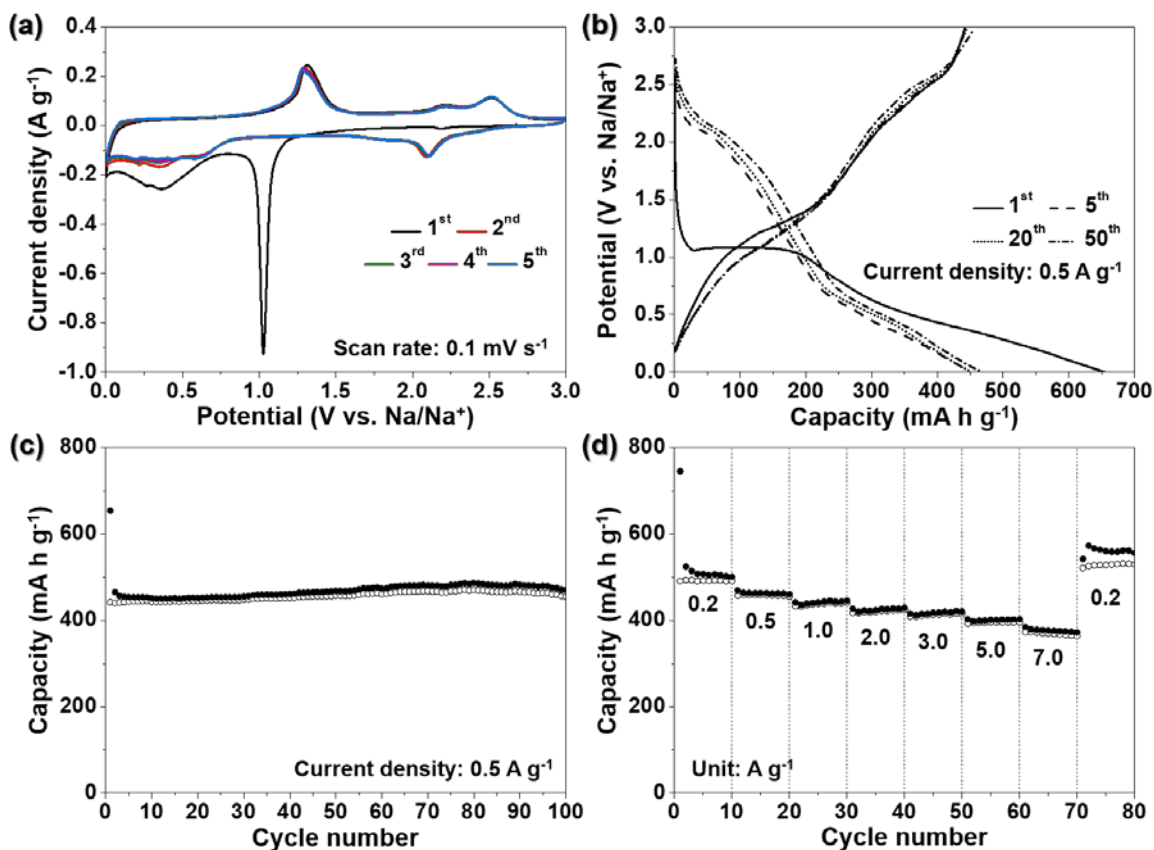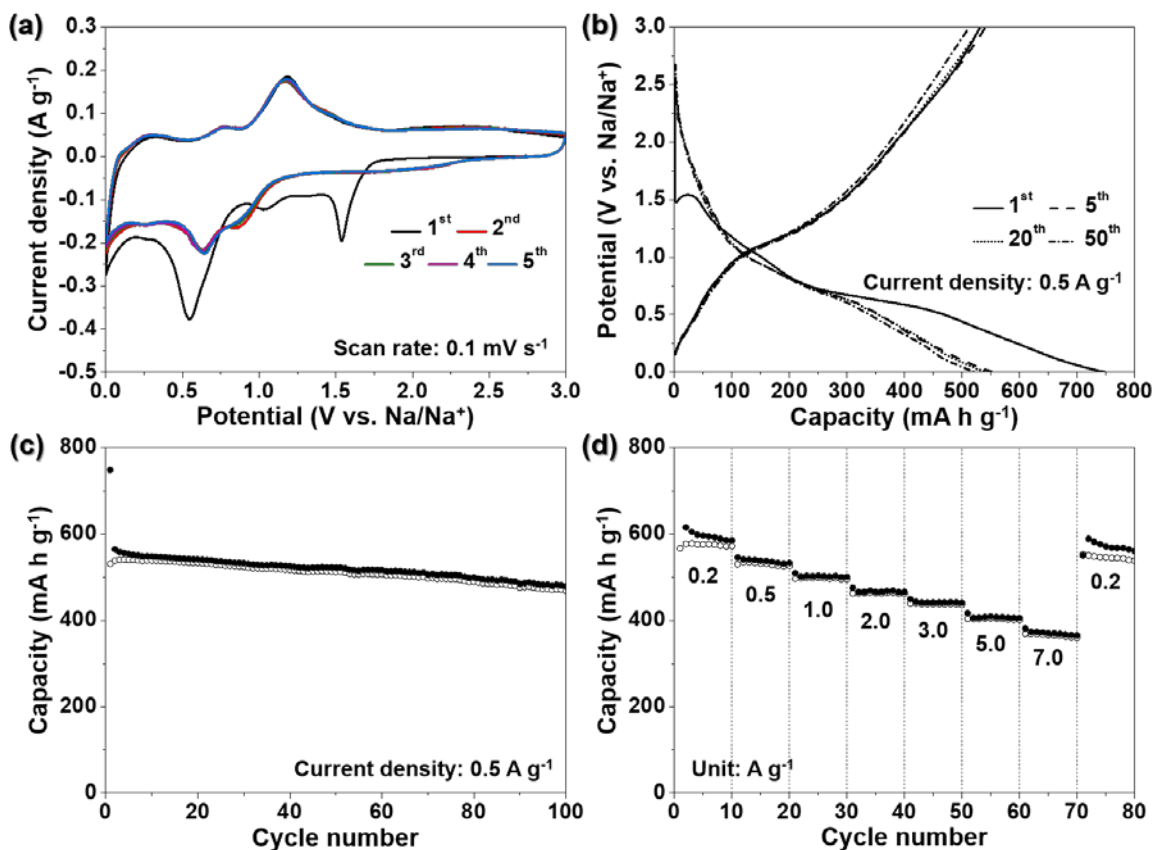
Fig. S18 Sodium-ion storage performances of SnS/C-NR: (a) CV curves for the initial 5 cycles, (b) discharge-charge profiles, (c) cycling performance at a current density of 0.5 A g^{-1}, and (d) rate performance.

In the first cathodic scan of the CV graph of SnS/C-NR (Figure S13a), the reduction peaks at 1.54 and 1.03 V was attributed to the conversion of SnS into Sn nanocrystals and Na$_2$S matrix, along with the formation of SEI layer. The sharp reduction peak at 0.54 V was attributed to the alloying reactions of Na and Sn to form Na$_x$Sn alloys. In the following anodic scan, the oxidation peaks at 0.29 and 0.74 V corresponded to the dealloying process of Na$_x$Sn to Sn metal. The other oxidation peaks at 1.18 and 1.40 V were assigned to the reversible conversion reaction.[S3,S4]

Table S1 Electrochemical properties of various nanostructured MoS_2-based anode materials for sodium-ion batteries reported in the previous literatures.

Morphology	Synthesis method	Voltage window [V]	Current density [A g^{-1}]	Discharge capacity [mA h g^{-1}] (Cycle)	Rate performance [mA h g^{-1}] (Curren density)	Ref.
Micro-MoS_2	Solid-state reaction	0.2-3	0.2	136 (70th)	112 (10 A g^{-1})	S5
MoS_2/C nanofibers	Electrospinning	0.01-3	0.1	284 (600th)	186 (2.0 A g^{-1})	S6
MoS_2 nanoflowers	Hydrothermal synthesis	0.4-3	1.0	300 (1500th)	175 (10 A g^{-1})	S7
Worm-like MoS_2	Solvothermal synthesis	0.01-3	0.062	411 (80th)	~50 (0.62 A g^{-1})	S8
Ultrathin MoS_2	Ultrasonic exfoliation	0.01-3	0.04	386 (100th)	251 (0.32 A g^{-1})	S9
Vine-like MoS_2 nanofiber	Electrospinning	0.01-3	0.1	600 (600th)	660 (2.5 A g^{-1})	S10
3D MoS_2-graphene microspheres	Spray pyrolysis	0.001-3	1.5	322 (600th)	234 (10 A g^{-1})	S11
3D MoS_2-rGO nanoflowers	Hydrothermal synthesis	0.01-2.6	0.5	318 (90th)	433 (1.0 A g^{-1})	S12
MoS_2/C nanospheres	Hydrothermal synthesis	0.005-2.5	0.067	400 (300th)	390 (1.34 A g^{-1})	S13
MoS_2/hierarchical porous carbon	Solventless process	0.01-2.9	1.0	280 (300th)	122 (10 A g^{-1})	S14

3D interconnected MoS$_2$@carbon nanofiber	Electrospinning	0.05-3	1.0	282 (600th)	412 (1.0 A g^{-1})	S15
MoS$_2$/C-multiwall CNT	Hydrothermal synthesis	0.005-3	2.0	416 (1000th)	324 (20 A g^{-1})	S16
MoS$_2$ nanosheets on amorphous CNT	Hydrothermal synthesis	0.005-3	0.5	461 (150th)	396 (1.6 A g^{-1})	S17
3D MoS$_2$@C framework	Melamine foam carbonization	0.05-3	1.0	240 (500th)	95 (10 A g^{-1})	S18
MoS$_2$/C with cubic nanorooms	*Spray pyrolysis*	*0.001-3*	*0.5*	*385 (350th)*	*287 (7.0 A g^{-1})*	*This work*

REFERENCES

(S1) Z. Liu, T. Lu, T. Song, X.-Y. Yu, X. W. D. Lou and U. Paik, *Energy Environ. Sci.*, 2017, **10**, 1576-1580.

(S2) A. Douglas, R. Carter, L. Oakes, K. Share, A. P. Cohn and C. L. Pint, *ACS Nano,* 2015, **9**, 11156-11165.

(S3) S. H. Choi and Y. C. Kang, *Nano Res.*, 2015, **8**, 1595-1603.

(S4) X. Xiong, C. Yang, G. Wang, Y. Lin, X. Ou, J.-H. Wang, B. Zhao, M. Liu, Z. Lin and K. Huang, *Energy Environ. Sci.*, 2017, **10**, 1757-1763.

(S5) X. Wang, Y. Li, Z. Guan, Z. Wang and L. Chen, *Chem. Eur. J.*, 2015, **21**, 6465-6468.

(S6) X. Xiong, W. Luo, X. Hu, C. Chen, L. Qie, D. Hou and Y. Huang, *Sci. Rep.*, 2015, **5**, 9254.

(S7) Z. Hu, L. Wang, K. Zhang, J. Wang, F. Cheng, Z. Tao and J. Chen, *Angew. Chem. Int. Ed.*, 2014, **53**, 12794-12798.

(S8) M. Xu, F. L. Yi, Y. Niu, J. Xie, J. Hou, S. Liu, W. H. Hu, Y. Li and C. M. Li, *J. Mater. Chem. A*, 2015, **3**, 9932-9937.

(S9) D. Su, S. Dou and G. Wang, *Adv. Energy Mater.*, 2015, **5**, 1401205.

(S10) W.-H. Ryu, J.-W. Jung, K. Park, S.-J. Kim and I.-D. Kim, *Nanoscale*, 2014, **6**, 10975-10981.

(S11) S. H. Choi, Y. N. Ko, J. K. Lee and Y. C. Kang, *Adv. Funct. Mater.*, 2015, **25**, 1780-1788.

(S12) T. S. Sahu and S. Mitra, *Sci. Rep.*, 2015, **5**, 12571.

(S13) J. Wang, C. Luo, T. Gao, A. Langrock, A. C. Mignerey and C. Wang, *Small*, 2015, **11**, 473-481.

(S14) S.-K. Park, J. Lee, S. Bong, B. Jang, K.-D. Seong and Y. Piao, *ACS Appl. Mater. Interfaces*, 2016, **8**, 19456-19465.

(S15) W. Li, R. Bi, G. Liu, Y. Tian and L. Zhang, *ACS Appl. Mater. Interfaces*, 2018, **10**, 26982-26989.

(S16) B. Chen, H. Lu, J. Zhou, C. Ye, C. Shi, N. Zhao and S. Z. Qiao, *Adv. Energy Mater.*, 2018, **8**, 1702909.

(S17) X. Xu, D. Yu, H. Zhou, L. Zhang, C. Xiao, C. Guo, S. Guo and S. Ding, *J. Mater. Chem. A*, 2016, **4**, 4375-4379.

(S18) Z.-H. Zhao, X.-D. Hu, H. Wang, M.-Y. Ye, Z.-Y. Sang, H.-M. Ji, X.-L. Li and Y. Dai, *Nano Energy*, 2018, **48**, 526-535.